Homogenisation of Slender Periodic Composite Structures

Julian Dizy, Rafael Palacios*, and Silvestre T. Pinho

Department of Aeronautics, Imperial College, London, SW7 2AZ, United Kingdom

A homogenisation technique is introduced to obtain the equivalent 1-D stiffness properties of complex slender periodic composite structures, that is, without the usual assumption of constant cross sections. The problem is posed on a unit cell with periodic boundary conditions such that the small-scale strain state averages to the large-scale conditions and the deformation energy is conserved between scales. The method can be implemented in standard finite-element packages and allows for local stress recovery and also for local (periodic) nonlinear effects such as skin wrinkling to be propagated to the large scale. Numerical examples are used to obtain the homogenised properties for several isotropic and composite beams, with and without transverse reinforcements or thickness variation, and for both linear and geometrically-nonlinear deformations. The periodicity in the local post-buckling response disappears in the presence of localisation in the solution and this is also illustrated by a numerical example.

Nomenclature

b = unit cell depth, m

$\mathcal{C}_{ijkl}$ = material elasticity tensor

θ_i = large scale local rotations, rad

E = Young's modulus, Pa

ϵ = beam strains

ε_{ij} = infinitesimal strain tensor

G = shear modulus, Pa

ν = Poisson's ratio

L = length of the beam, m

Ω = volume of the unit cell, m^3

* *Corresponding author:* Room 355, Roderic Hill Building, South Kensington Campus; E-mail address: rpalacio@imperial.ac.uk; Tel: +44 20 7594 5075.

$\mathcal{S}$ = homogenised 4×4 stiffness matrix

$\mathcal{U}$ = elastic strain energy, J/m

u_i = large scale local displacements, m

v_i = small scale displacement field, m

w_i = warping field, m

1. Introduction

Despite significant advances in computational power in the last decade, which allow direct solid modelling of most engineering structures, there is still a practical interest in dimensionally-reduced structural models. Beam models, in particular, provide excellent approximations of the primary structures for low-frequency aeroelastic analysis of high-aspect-ratio wings, helicopter rotor blades or wind turbines. A review of the available analysis methods was presented by Palacios et al., (2010). They have also proved to be very useful in the study of carbon nanotubes (Li and Chou, 2003), marine riser pipes (Kaewunruen et al., 2005) and proteins (Leamy and Lee, 2009), among others. The simplicity of construction of the models also makes them essential tools in many other applications for conceptual studies. A great deal of effort has been put into developing composite beam models (Hodges, 2005), able to account for elastic couplings in reduced one-dimensional models. In general, the modelling process can be split into two different stages: Firstly, there is a *homogenisation step*, which determines the constitutive relations of the reduced model (i.e., beam sectional properties); secondly, there is a *solution step*, in which one evaluates the response of the dimensionally-reduced model to the set of applied loads. Both stages are interrelated as assumptions on one affect the other. The equations of motion in the *solution stage* have been well developed, including geometrically-nonlinear effects, in the works of, for instance, Simo and Vu-Quoc (1986); Cardona and Geradin (1988) and Hodges (1990; 2003). The constitutive relations in that first stage, which will be the focus of this work, have been mostly obtained under the assumption of constant (or slowly-varying) cross sections.

For composite beams, one of the most successful approaches in dealing with arbitrary sectional properties is the Variational Asymptotic Method (VAM) (Cesnik and Hodges, 1997). The analysis asymptotically approximates the 3-D warping of the displacement field that minimizes the cross-sectional deformation energy for each beam strain state and thus finds the constitutive relations for the 1-D beam analysis. After the global deformation from the 1-D (possibly nonlinear) beam analysis is obtained, the original 3-D displacements, stresses and strains can also be

recovered using those 3-D warping influence coefficients. It is worth noting that solutions based on VAM only apply to the interior solutions in constant-section beams.. Very recently, Lee and Yu (2011) have proposed, as a partial remedy to that shortcoming, to use the smallness of the heterogeneity and incorporate a spanwise dimensional reduction, in the homogenisation step of the variational asymptotic method. The resulting formulation is then similar to that obtained by the Formal Asymptotic Method (Buannic and Cartraud, 2001a, b; Kim and Wang, 2010), which exploits the existence of two scales in the original dynamic 3D equations governing the elastic response of the beam structure to perform an asymptotic homogenisation. However, it is not always apparent in the original formulation how to define an adequate set of boundary conditions, implementing it numerically or adapting it to conventional engineering models. This was later remedied by Cartraud and Messager (2006), which restricted the solution to the four "classical" beam elastic states (axial, torsion and bending in two directions). The resulting problem was then implemented in a commercial finite-element package (Samcef). This work resulted in an approach similar to that of Ghiringhelli and Mantegazza (1994), who had modified a finite element software's matrix solving procedure in order to obtain the beam section properties.

A further possibility is that proposed by Kennedy and Martins (2012), which builds a kinematic description of the beam from a linear combination of fundamental state solutions. The first fundamental solutions are axially-invariant, and their corresponding deformation state is calculated at the mid plane of the beam by using a 2D finite-element method to obtain the stresses and strains due to the Saint-Venant (axial, bending, torsion and shear) (Ieşan, 1986a) and Almansi-Michell (distributed surface load) loadings (Ieşan, 1986b). This method yields solutions with accuracy comparable to that of full 3-D analysis using the Finite-Element Method (FEM) as long as the sections do not vary along the axis of the beam and the loads are statically determined. A similar superposition method is used by Jonnalagadda and Whitcomb (2011) to calculate the transverse shear components of the stiffness matrix. Their approach is based on applying to the section a bending moment equal in magnitude, but with opposite sign, than that created by the shear force. This is presented for isotropic structures of constant cross sections.

The previous solutions either were limited to constant-section geometries, required dedicated –and often quite involved– implementations, or user-created modules or subroutines in a standard finite-element solution package. Furthermore, the mentioned methodologies are linear approaches that therefore only provide strength estimates based on linear stress and strain distributions. Due to their high strength-stiffness ratio, composite thin wall structures usually exhibit local or distortional buckling before material failure (Qiao and Shan, 2005) and this is

often a design constraint. Consequently, the objective of the present work is twofold: 1) to introduce a general methodology to evaluate both the elastic constants and local buckling characteristics, such as skin wrinkling (Su and Cesnik, 2011), of composite beams with spanwise periodic properties; and 2) to define in such a way that can be implemented into a general-purpose finite-element code, thus taking advantage of all the advanced modeling features of the leading commercial packages. Similarly to the work of Lee and Yu (2011) and Cartraud and Messager (2006), the methodology will be based on the static analysis of a unit cell, which will be assumed to be much smaller than the characteristic wavelength in the beam response. The final equations to obtain the beam stiffness matrix have been solved using periodic boundary conditions in an off-the-shelf finite-element solver (Abaqus) and with models which are assembled using tie constraints from substructures with non-coincident nodes, which considerably simplifies model generations with a negligible impact on the homogenised properties. The solution method is finally extended to certain geometrically-nonlinear (but still periodic) problems.

2. Theory

Consider a slender prismatic solid made by repeating a periodic cell along its longitudinal dimension – – (see Figure 1). The transverse dimensions of the structure, *h* are much smaller than the characteristic longitudinal dimension . The coordinate *y* in the reference configuration defines the reference line for the 1-D large scale (beam) which coincides with the neutral axis. The longitudinal dimension of the cell is . To obtain the homogenised elastic constants, linear assumptions are used for the kinematics and the local material properties.

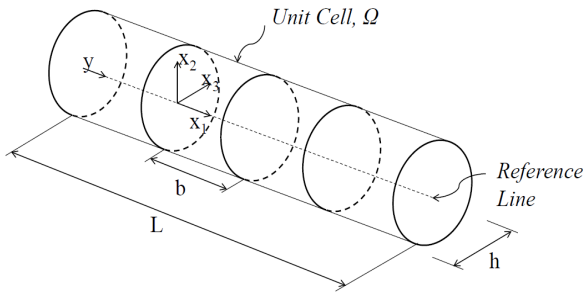

Figure 1: Schematic diagram of a slender periodic structure with unit cell representation.

The adopted solution relies on two assumptions made between scales to deduce a set of periodic boundary conditions and obtain the beam stiffness constants (Geers et al., 2010). These assumptions are: a) the large scale (macroscopic) variables ( ) are averages of the small scale (microscopic) ones (, and b) the deformation

energy is conserved between scales. The large scale is associated with the 1-D beam level as described above, and the small scale is associated with the dimensions of the cross section (x_2 and x_3) and the unit cell (x_1). The formulation described here is a first-order theory and does not include the effects from transverse shear. All throughout this section, Einstein notation is used for repeated indices, with Latin indices assuming values from 1 to 3 and Greek ones assuming values of 2 and 3.

2.1. Kinematics

Under linear assumptions, the deformation of the reference line can be described by three local displacements $u_i(y)$ and three local rotations $\theta_i(y)$ along the axes x_i of the coordinate system in Figure 1. The beam strain measures are obtained from linearization of the strain-displacement kinematic relations in Palacios et al. (2010), as

$$\begin{aligned} \gamma_1(y) &= u_1', \\ \gamma_\alpha(y) &= u_\alpha' - e_{\alpha\beta}\theta_\beta, \\ \kappa_i(y) &= \theta_i', \end{aligned} \tag{1}$$

with $e_{\alpha\beta}$ being the Levi-Civita or permutation symbol. If we further assume $\gamma_\alpha(y) = 0$, i.e., a first-order theory, that implies

$$\theta_2 = -u_3';\ \theta_3 = u_2'. \tag{2}$$

We define the vector of first-order beam strains containing extensional strain γ_1, bending curvatures in two directions κ_2, κ_3 and torsional curvature κ_1, as

$$\epsilon^{\mathrm{T}} = \{\gamma_1 \quad \kappa_1 \quad \kappa_2 \quad \kappa_3\}. \tag{3}$$

At the small scale level, we consider the 3-D deformation of a cell of volume Ω centred at *y* (see Figure 1). The undeformed position within the cell will be given by coordinates x_i, where x_1 is parallel to y, but measures lengths at cell scales (i.e.,$\frac{dx_1}{dy} = \frac{b}{L}$) and it can be seen as magnified coordinate system. The three components of the small scale displacement field are $v_i(y; x_1, x_2, x_3)$. The two longitudinal dependencies are introduced to separate between *small scale* ($\sim x_1$) and *large scale* fluctuations ($\sim y$) of the structural deformations (Lee and Yu, 2011). The warping field, w_i, is then defined as the difference between the small and large scale displacement fields, as

$$v_1(y;x_1,x_2,x_3) = u_1(y) - e_{\alpha\beta}x_\alpha\theta_\beta(y) + w_1(y;x_1,x_2,x_3),$$
$$v_\alpha(y;x_1,x_2,x_3) = u_\alpha(y) - e_{\alpha\beta}x_\beta\theta_1(y) + w_\alpha(y;x_1,x_2,x_3), \quad (4)$$

Note that if the warping field is zero, Eq. (4) is the kinematic assumption used in Timoshenko beam theory (or Euler-Bernoulli theory if the condition of Eq. (2) is enforced) which has been referred to as the *fundamental solution* in asymptotic theories (Kim and Wang, 2010). In general the warping field will depend on the cell and correspondingly it was explicitly written as a function of the spanwise coordinate, y.

The independent large scale variables are defined from averages in the cell, as

$$u_i(y) = \langle v_i \rangle,$$
$$\theta_1(y) = \frac{1}{2}\langle v_{3,2} - v_{2,3} \rangle, \quad (5)$$

where $\langle \bullet \rangle = \frac{1}{\square}\int_{\square} \bullet \, dx_1 dx_2 dx_3$ and $\bullet_{,j} = \frac{\partial \bullet}{\partial x_j}$. If we take the reference axis at the centroid, i.e. $\langle x_\alpha \rangle = 0$, then these definitions impose four constraints on the warping field,

$$\langle w_i \rangle = 0,$$
$$\langle w_{2,3} - w_{3,2} \rangle = 0. \quad (6)$$

2.2. Equilibrium conditions

Our interest is in the interior solution of the problem to obtain the 4×4 homogenised stiffness matrix, $\mathcal{S}$, and these can be obtained simply by assuming constant large scale strains, that is, $\epsilon(y) = \bar{\epsilon}$. We then postulate constitutive relations in the homogenised problem such that the strain energy is conserved between the small and large scale levels (Geers et al., 2010). Due to the periodicity of the problem, the small scale strain energy per unit beam length is independent of the cell in the interior solution, and it is

$$\mathcal{U} = \frac{1}{2}\bar{\epsilon}^T \mathcal{S} \bar{\epsilon} = \frac{1}{2b}\int_\Omega \mathcal{C}_{ijkl}\varepsilon_{ij}\varepsilon_{kl} dx_1 dx_2 dx_3, \quad (7)$$

with $\mathcal{C}_{ijkl}(x_1,x_2,x_3)$ being the material elasticity tensor and $\varepsilon_{ij} = \frac{1}{2}(v_{i,j} + v_{j,i})$ the components of the small scale strain tensor. Define now the magnitudes $\Delta v_i = v_i\left(y;\frac{b}{2},x_2,x_3\right) - v_i\left(y;-\frac{b}{2},x_2,x_3\right)$. Eq. (4) becomes

$$\Delta v_1(y; x_2, x_3) = \bar{\gamma}_1 b - e_{\alpha\beta} x_\alpha \bar{\kappa}_\beta b + \Delta w_1(y; x_2, x_3)$$
$$\Delta v_\alpha(y; x_2, x_3) = -e_{\alpha\beta} x_\beta \bar{\kappa}_1 b + \Delta w_\alpha(y; x_2, x_3). \quad \textbf{(8)}$$

For this solution to be independent of the cell, it must be $\Delta w_i(y; x_2, x_3) = 0$, i.e., the warping field is periodic. This can also be concluded arguing that, due to periodicity, the strain field must be compatible and the only difference in displacement allowed between both faces of the cell is a rigid body motion, which does not create strain. We are finally left with the problem of obtaining the static equilibrium conditions on a generic cell under an applied displacement field given by

$$v_1\left(\tfrac{b}{2}, x_2, x_3\right) = v_1\left(-\tfrac{b}{2}, x_2, x_3\right) + \bar{\gamma}_1 b - e_{\alpha\beta} x_\alpha \bar{\kappa}_\beta b,$$
$$v_\alpha\left(\tfrac{b}{2}, x_2, x_3\right) = v_\alpha\left(-\tfrac{b}{2}, x_2, x_3\right) - e_{\alpha\beta} x_\beta \bar{\kappa}_1 b. \quad \textbf{(9)}$$

where the reference to the long-scale coordinate, y, is no longer necessary. This problem can be set up in any standard FEM solver using multipoint constraints to enforce the periodic boundary conditions defined by Eq. (9) Ten different combinations of loading cases are then considered, corresponding to unit values in each of the four components of the beam strain $\bar{\epsilon}$, and unit value in each of the six possible different pairs of strains (e.g., coupled axial/torsion, axial/x_2-bending, and so on). For each load state, the strain energy per unit length is then computed from the solved model using the right hand side of Eq. (7), which is then used to solve the 10 independent coefficients of the stiffness matrix, $\mathcal{S}$.

2.3. Extension to geometrically nonlinear, periodic formulation

The previous formulation can be directly extended to geometrically-nonlinear problems in two situations: Firstly, when the nonlinear effects appear in the macroscopic scale but relative displacements are still small at the local (cross-sectional) scale; and secondly, when there are geometrically-nonlinear effects at the cell level but the solution is still periodic. The first problem can then be seen as a linearization around a different reference condition but it remains fundamentally unchanged. This is the problem encountered in geometrically-nonlinear beam modelling with constant (elastic) stiffness matrices (Cesnik et al., 1996). A more interesting situation appears in the second scenario, when there are geometrically-nonlinear effects at the cell level *and* all the cells in the structure deform equally. A

relevant example of this corresponds to the panel buckling (or skin wrinkling) in aircraft wings. If all cells are under the same loading, as it is assumed in the homogenisation procedure, then buckling will simultaneously initiate in all cells. The periodicity will then hold until localisation occurs (Pinho et al., 2006). This will be numerically exemplified in the section 4.3.

Assuming that the cell undergoes large local displacements (relative to the typical cell dimension, h) but that the 1-D beam displacements are still linear (the length scale there, L, is still very large), then the local 3-D strains obtained from the geometrically-nonlinear solution on the cell can be used to obtain the current beam stiffness. In this case, the local 3D strains are calculated in the deformed geometry and the volume integral in the strain energy calculation of Eq. 7 corresponds to the current configuration. In this paper, we will further assume that the end sections of the cell, at $x_1 = \pm\frac{b}{2}$, do not have large relative rotations, and therefore the periodic boundary conditions defined by Eq. (9) remain unchanged (this occurs, for instance for the local buckling analysed in section 4.3). For the more general cases that still show periodicity of the warping field, but also include large relative rotations between the end cell sections, a more general formulation would be required. This is however beyond the scope of this work.

3. Numerical implementation

There are four basic steps involved in the implementation of the homogenisation procedure described above into the finite element software Abaqus (SIMULIA, 2010). The solution process has been schematized in Figure 2:

I. The geometry of the cell is created using a Python script whose inputs are cell dimensions, mesh density, material properties and type of analysis. Using this data, an Abaqus standard input file is generated including a set of periodic boundary conditions from Eq. (9). Each loading case is introduced via a different (fictitious) *master node* for which prescribed displacements are applied.

II. The model is meshed using 'C3D8R' (3D-cuboid-8node) elements with reduced integration for the calculation of the linear stiffness properties and full integration 'C3D8' in the case of a buckling analysis or complicated geometries. This is due to the complexity of buckling deformed shapes and hence the likelihood of hourglassing and other convergence problems. For the anisotropic cases, each element has its own local coordinate system that defines the ply orientation (each composite ply is modelled with a layer of elements). For the homogenisation step, details such as stress concentrations at joints have a very small effect in the beam stiffness constants and therefore the meshing can be done independently for the various

subcomponents of the cells (e.g. rib, spars, skin in a wing example), which are finally linked via tie constraints in the Abaqus model (SIMULIA, 2010). This gives a big flexibility to the generation of the FEM model.

III. The requested set of analyses is then performed: standard linear elastic with ten load cases –corresponding to each of the loadings (extension, twist, bending in both directions) and the pair-wise combinations of these–, a linear perturbation buckling analysis or a fully nonlinear analysis.

IV. Then the Abaqus output database (.odb) file generated from the analysis is read automatically. This step further justifies the use of Python as Abaqus uses this language internally for analysis and database organization. Finally, the elastic strain energy is integrated for the whole model and using Eq. (7) the stiffness matrix is calculated for the unit cell.

Note that this approach is however independent of the particular scripting language or FEM package used. All the information can be written into a standard Abaqus model and the solution procedure requires no user-defined modules in the FE solver.

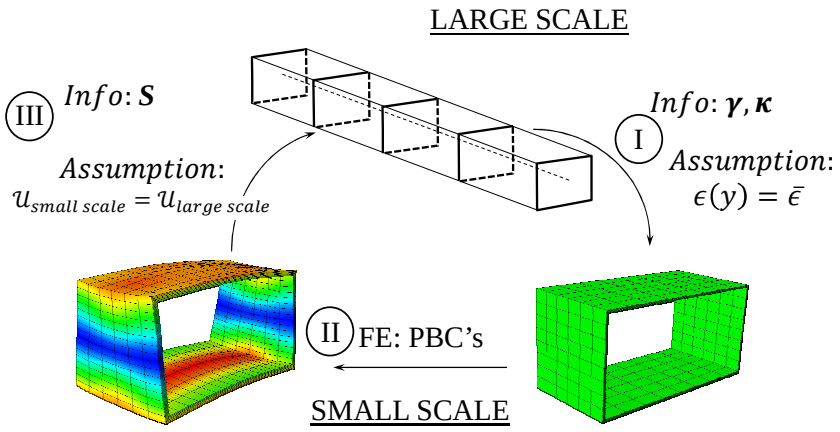

Figure 2: Flow of information between the large and small scales

4. Numerical studies

The methodology described above is exemplified here via four case studies of increasing complexity. The first case (section 4.1) is a model of a prismatic isotropic box-beam that includes transverse reinforcements. The second case is based on a laminated thin-walled cylinder used to substantiate the implementation of composite materials and

compare the results to those obtained using UM/VABS (Palacios and Cesnik, 2005); then, 3D solutions are considered with periodic variations of the wall thickness. The third case (section 4.3) introduces the local buckling strain prediction and evaluates the residual post-buckling stiffness. Finally, section 4.4 shows a composite rotor blade section that is used to illustrate effective complex sectional modelling using tie constraints.

4.1. Isotropic prismatic box beam with transverse reinforcements

This first model is a ribbed prismatic box beam made out of homogenous isotropic material (aluminium: E=70GPa, ν=0.3) with width and height equal to 2m and 1m, respectively, and with 0.025m-thick walls. The distance between ribs is b=1m, which defines the unit cells. In order to define a reference for comparison, a full box-beam of length L=20m is built-in on one end and all the loads or moments are applied via a rigid body node-constraint and a reference point at the other end. The full model is meshed using 10400 C3D8R elements with 17421 nodes and is partially shown in Figure 3 (a cut-out has been included for better visualization). The unit cell mesh has

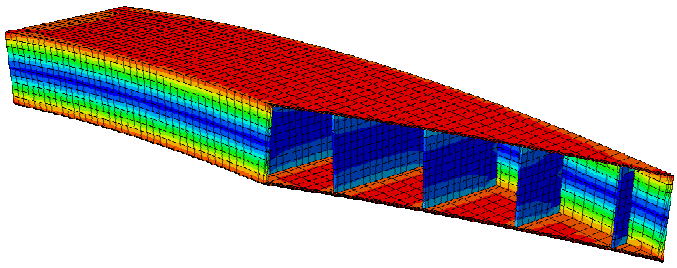

Figure 3: Vertical cut-out of the deformed reinforced box-beam model under tip moments (κ_3=0.1m^{-1}). Contour plot shows von Mises stress

a twentieth of that number. There are ten elements along the height, width and span of one cell, and three through the thickness. The transverse reinforcements in both models (full and unit cell) are added to the model via tie constraints, which avoids local mesh refinement in the joints between rib and outer skin. The geometry and the von Mises stress contour of the full structure subject to a tip bending moment (κ_3=0.1m^{-1}) are shown in Figure 3.

Stiffness results are summarized in Table 1 and compared with results without ribs obtained by: a) analytical results from thin-walled beam theory; b) full 3D FEM analysis using static loading; c) UM/VABS. The last column shows the effect of adding a transverse rib of the same thickness of the outer walls at the cells' mid-span position.

The agreement of the results produced by this homogenisation method is excellent both with the theory and the current available tools. The small discrepancy that thin-wall theory has, in the case of torsion, with both UM/VABS (Palacios and Cesnik, 2005) and the proposed method, is due to the thin-wall assumption of the former. The addition of the transverse wall results in a small change, which can nevertheless be estimated with the present approach.

Table 1: Homogenised stiffness constants for the prismatic box beam.

Stiffness constant	No ribs				With ribs	
	Analytical (Thin wall)	FE (full beam)	UM/VABS	Present method	FE (full beam)	Present method
$S_{11}(EA)$ [GN]	10.3	10.3	10.3	10.3	10.5	10.5
$S_{22}(GJ)$ [GNm²]	1.79	1.71	1.71	1.71	1.72	1.72
$S_{33}(EI_{33})$ [GNm²]	1.91	1.91	1.91	1.91	1.94	1.94
$S_{44}(EI_{22})$ [GNm²]	5.58	5.58	5.58	5.58	5.62	5.62

4.2. Laminated cylinder with constant ply angle and span-wise variable thickness

Two subcases are considered: a 2-ply, constant-fibre-orientation-angle circular cylinder, which will be used to demonstrate the stiffness variation as the ply angle changes; and a modified section of this, that will be used to exemplify the approach for cross sections of varying thickness along the span. Material orientations are taken clockwise around the circumferential direction of the tube, with the x_1 direction as the reference for a zero degree ply angle.

Table 2: Ply properties of the laminated cylinder

E_{11}=1.42×10¹¹ Pa	E_{22}= E_{33}=9.8×10⁹ Pa
G_{12}=G_{13}=6.0×10⁹ Pa	G_{23}=4.8×10⁹ Pa
ν_{12}= ν_{13}=0.3	ν_{23}=0.3

For the reference (constant-section) case, the cylinder has unit radius, R=1m, measured to the outer wall, and 5% thickness (t=0.05m), as depicted in Figure 4. The length of the unit-cell model, which does not affect the

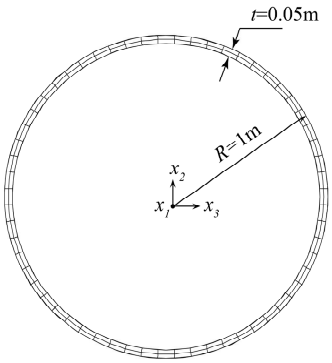

Figure 4: Cross-sectional discretization and dimensions of the reference laminated cylinder. (Cell model is 3-D.)

homogenised results, is b=0.1m. This has been meshed with 320 C3D8R elements (724 nodes). There are two elements per 9 degrees, one per ply and two in the span direction (only one is needed). The material properties of the composite used are given in Table 2.

The non-zero terms of the 4x4 stiffness matrix have been plotted in Figure 5 together with the results obtained using UM/VABS (Palacios and Cesnik, 2005). These terms include: extensional (S_{11}), torsional (S_{22}), and bending (S_{33}) stiffnesses plus the coupling between the first two (S_{12}). Only one bending stiffness is shown in the figure, as the section is symmetric. The evolution of these constants with the ply angle agrees very well between both methods and the error is always less than 0.1%.

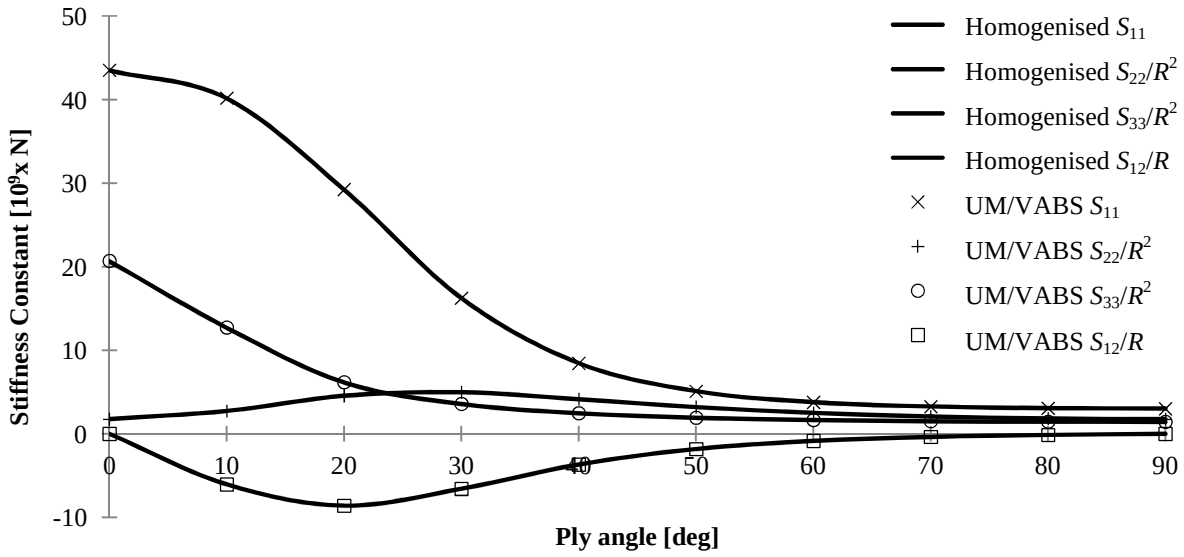

Figure 5: Stiffness constants as a function of the ply angle for the laminated cylinder with constant wall thickness.

A modified version of the previous example will be used next to explore the capabilities of the method to model 3D cells that include heterogeneity along the x_1 direction. For that purpose, the outer radius will remain the same, but the thickness of the section will vary as a function of the span-wise position, as shown in Figure 6. This change

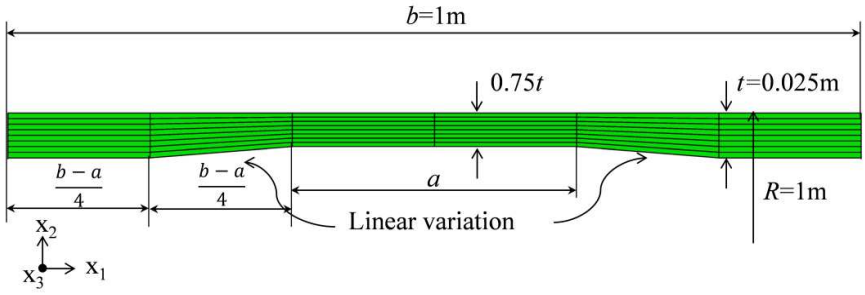

Figure 6: Longitudinal cut of the cell of the laminated cylinder showing the thickness variation

consists of a 25% reduction in thickness of the inner sections (length *a*) with a linear variation region joining the outermost sections which remain the same thickness. The material properties are those from Table 2. The composite layup is now a $[45,-45,0,90]_s$. The new mesh has 6 elements in the spanwise direction, one per ply (8 plies) and 50 in the azimuth coordinate. The unit-cell results will be compared to a full size linear FE analysis of a 10-cell beam created with a tessellation of the cell just described, which results in a rather large mesh with 24000 C3D8R elements. It is clamped on one end and loaded with a $_3$=0.1 m^{-1} equivalent bending moment applied on the other

end. It is worth noting that the unit cell model runs in seconds but the full-size model requires over *16GB of RAM* and takes two orders of magnitude longer to run. Figure 7 shows how the top nodes ($x_2=R$, $x_3=0$) deflect as a function of x_1 in the full model as compared to the deflection of a beam of the homogenised stiffness under the same load. Both solutions are very close with minor discrepancies at the boundaries of the beam, since *end effects* are not accounted for in the homogenised model. Table 3 contains the von Mises stress values through the thickness of all the plies at a 45º angle cut ($x_2=x_3=\sqrt{2}/2$m) at the mid-span location ($x_1=b/2$). It corroborates that the technique not only predicts homogenised stiffness and displacements correctly, but it also provides small scale stress levels across the plies of the periodic structure.

Table 3: Interpolated von Mises stress values across plies at mid-span nodes on varying-thickness cylinder – –

Ply angle [deg]	von Mises stress [MPa]	
	Homogenized	FE (full beam, centre cell)
45	400.0	400.5
-45	386.0	386.5
0	910.1	910.3
90	211.2	210.9
90	209.1	208.8
0	780.2	780.9
-45	283.7	278.9
45	233.4	239.0

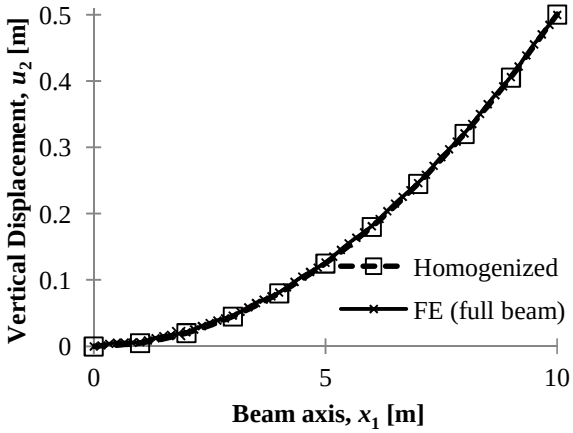

Figure 7: Vertical deflection of the top nodes of the varying-thickness cylinder – –

Given the level of automation of the mesh generation it is easy to perform a parametric analysis to check the sensitivity of the structure to variations of one (or more) of its variables. In this case, the effect of the thickness of the wall has been studied. This is done by increasing the relative length of the thin region (25%-reduced thickness part) with respect to the total length, *b*. The results are plotted in Figure 8. Note that in the limit when *a/b*=1 this corresponds to a cylinder of constant thickness 0.75*t*. The evolution of the stiffness constants follows an expected mild decrease as the thickness is reduced.

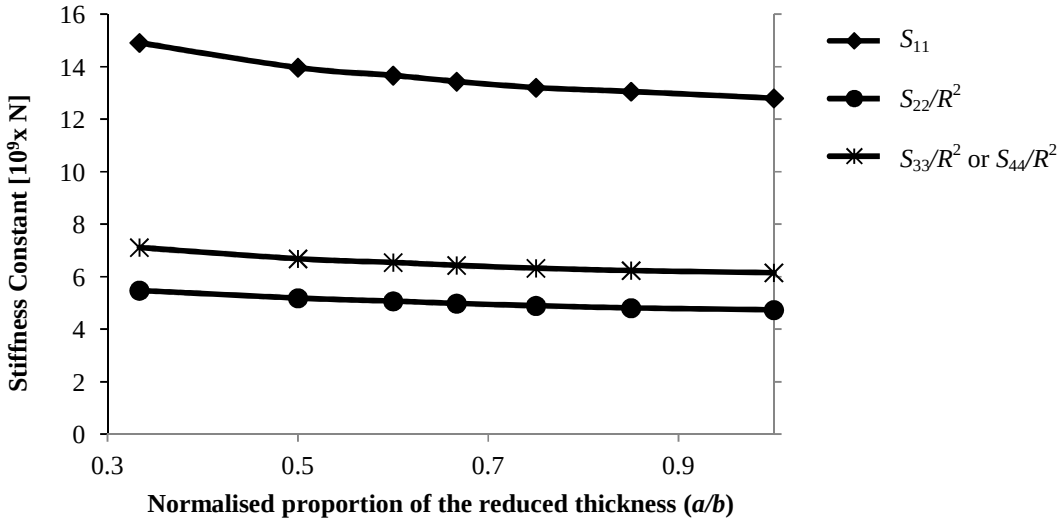

Figure 8: Effect of local thickness reduction on the stiffness of the laminated cylinder

4.3. Local buckling of a reinforced prismatic box beam

This case explores the suitability of a unit cell analysis to obtain local buckling loads under compressive forces when the solution is still periodic. Global buckling is not accounted for here but could instead be computed by the homogenised beam model. The model used is similar, in shape, to that of the first case (section 4.1), a prismatic box beam with perpendicular wall reinforcements, but the thicknesses of the skin and the reinforcement have been modified to ensure skin-buckling response. The new thicknesses are hence: 1mm for the skin and 10cm for the transverse reinforcement. All other model properties are kept the same as in the aforementioned case. From a convergence test, the full beam mesh is created with 24000 C3D8R elements, while the model of unit cell one is a sixth of that, that is, 4000 elements. All elements have a characteristic length of 10cm and there is 3 through the thickness in the skin and 2 in the wall. As it can be seen from Figure 9(b), the buckling mode of the structure is

coincident in both models –the unit cell and the full 3D one. The maximum displacement is in both cases normalised to one, and the magnitude of the axial strain at which local buckling occurs (eigenvalue) is found to be very close: =3.042 10^{-3} for the full 3D model and =3.058 10^{-3} for the unit cell It is clear that both approaches find the same solution for the first buckling mode.

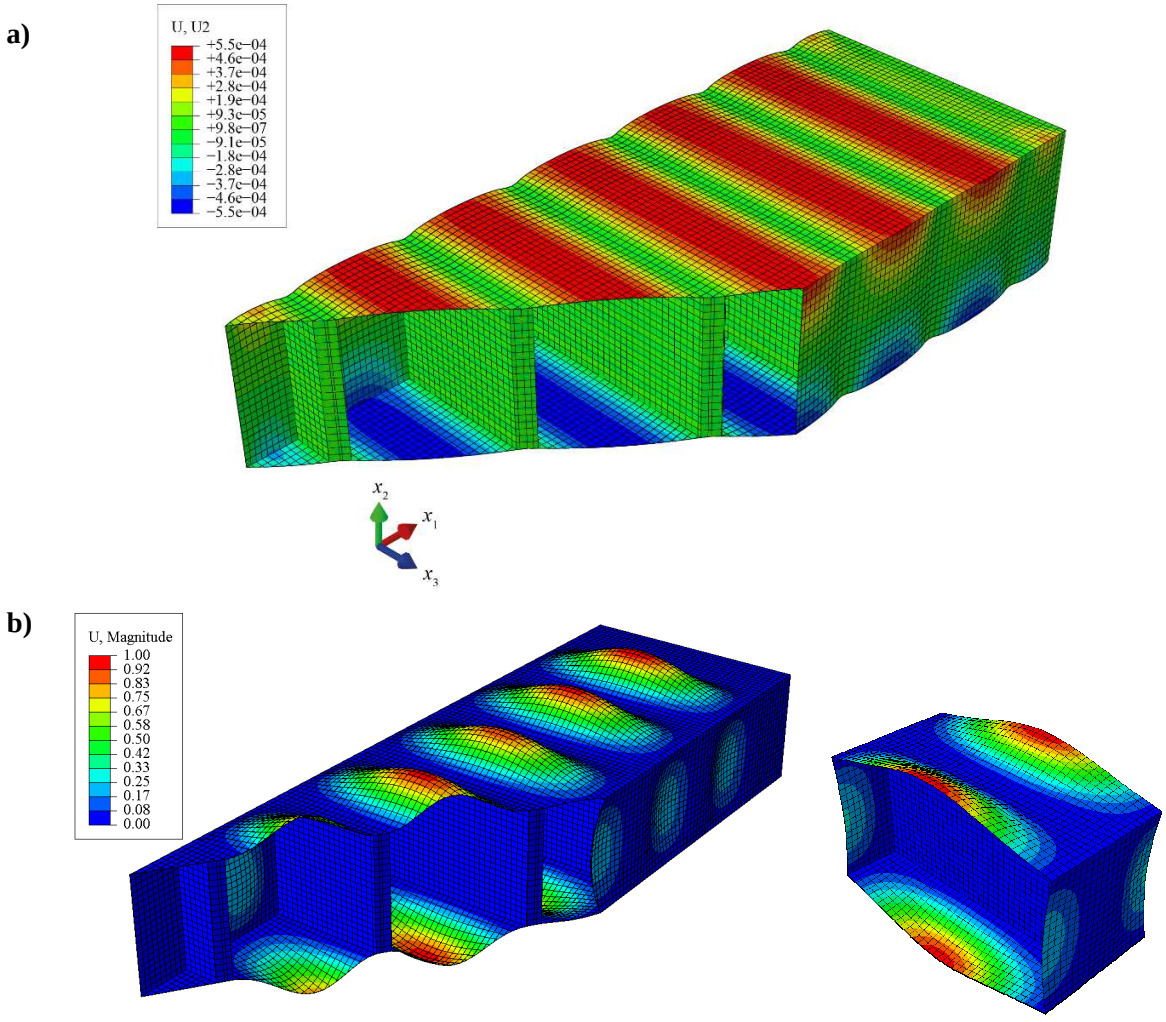

Figure 9: a) Vertical displacement in a *linear* ribbed prismatic beam subject to a compressive load of ; b) Contour plot of the first eigenshape of a ribbed prismatic beam under compressive loads. Full 3-D model (with a cut-out) shown on the left and unit cell on the right.

A geometrically-nonlinear analysis is then performed on the same model (with C3D8, full-integration elements) to compute its post-buckling stiffness. Please note that this is only valid on the assumption that all cells deform the same and hence the periodicity of the structure is not broken. Figure 10 shows the vertical displacement at the centre

top node of the horizontal top wall, as a function of the axial strain. Note that the displacement shown in Figure 10 is relative to the displacement at the end of the application of the perturbation load (if any is applied). Results are normalized with of the unit cell. The deflection at that node starts to diverge shortly after the normalised strain is unity, in agreement with the linear buckling analysis. The plot depicts three different load paths: one for the original structure and two corresponding to configurations with point normal loads of 500N and 1000N (positive inwards). The point forces are applied at the node where the displacement is measured, and in an antisymmetric manner; that is, the reciprocal node in the lower wall has the same load magnitude but opposite sign. The buckling of the original structure occurs with the horizontal walls buckling outwards and the side walls inwards (see Figure 9b) naturally, that is, without the need of a perturbation load. The deformation before buckling, shown in Figure 9a for a linear analysis with , leads to a non-uniform displacement field which triggers the bifurcation shown in Figure 10. For large enough perturbation loads (1000N in the example) vertical displacements in the opposite direction are obtained but the bifurcation load remains unchanged.

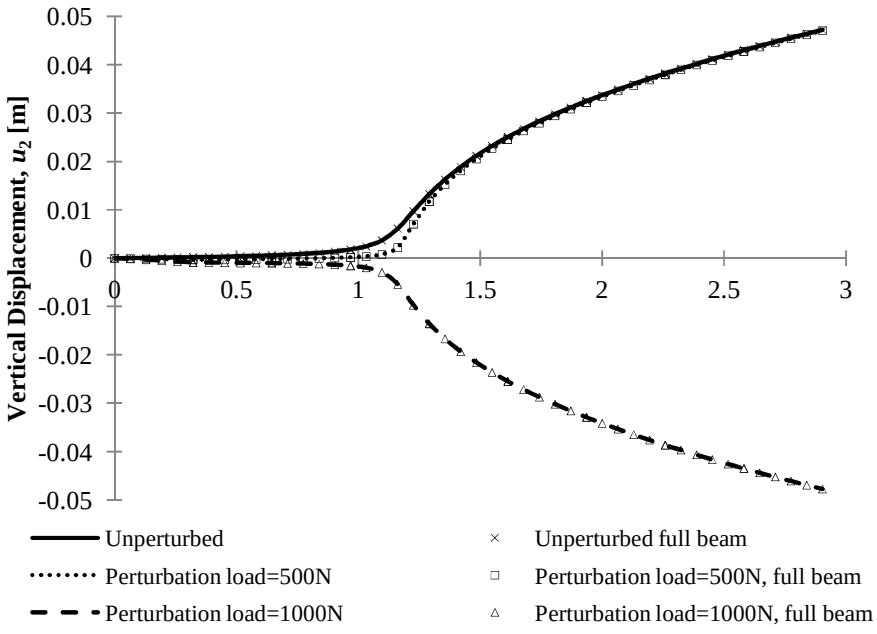

Figure 10: Nonlinear load path as a function of axial strain

The same energy-based procedure used in the linear case can be applied to each increment in the nonlinear step in order to calculate the stiffness constants as a function of a given loading or strain. In Figure 11, the axial (secant) stiffness, $S_{11,secant}$, has been computed for the axial deformations of up to 10% strain and three different wall thicknesses. This stiffness is calculated applying the same procedure described at the end of section 2.2 to each of

the increments in the nonlinear analysis in absolute terms. As the thick transverse reinforcements act as essentially rigid supports, the buckling strain is almost independent of the wall thickness. The nominal-thickness unit cell has also been compared with a full 3-D model, created with seven cells. As in previous cases, the boundary conditions on the full 3-D model are: encastre on one side and rigid body plus reference point (to apply the loading displacement and measure the reaction force) on the other. The results agree well but, as expected, the full model is slightly stiffer than the unit cell. This can be partially attributed to end effects in the full beam model. In addition, it can be observed that a negative tangent stiffness (slope of the load strain curves in Figure 12) is obtained at high strains, which implies that *localisation* has occurred (Pinho et al., 2006). Consequently, past this point ($\gamma_1$greater than $\sim$0.1), the assumption of periodicity is broken and the cell-based solution diverges from the actual response. In this particular example, with very thick transverse reinforcements, the cell model still gives a reasonable approximation, but this will not be the case in general. Continuing with the analysis of this example, when the tangent stiffness becomes zero, the beam response is no longer periodic and one of its cells will greatly deform, without increasing the load, while the others relax and go back to a lesser strain. In Figure 12, the reaction force and the axial component of the tangent stiffness have been plotted versus the axial strain in order to better understand the sequence of events in this localisation process. Before localisation, the strain in all unit cells (depicted in Figure 13a-b for $\gamma_1 = 0.05$) is the same. The load is always constant through the cells. When the tangent stiffness becomes negative ($\gamma_1 \cong$0.1), one of the cells will continue loading (growing γ_1, see Figure 13c) and the others will unload (decreasing γ_1, see Figure 13d). Note that after localisation has occurred, for a given load, various strain states are possible.

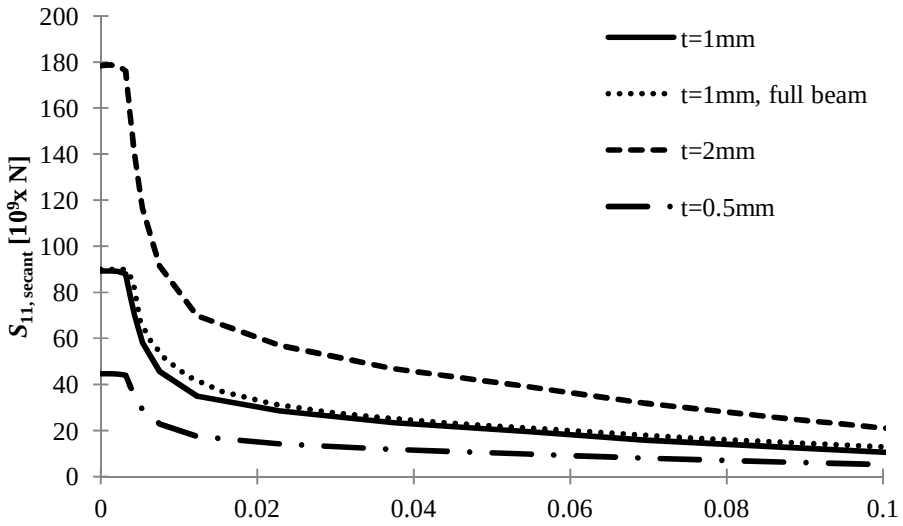

Figure 11: Post-buckling axial softening of the reinforced prismatic beam for various wall thicknesses

Note that a single unit cell with periodic boundary conditions predicts the conditions of the centre cell rather accurately thanks to the thickness of the transverse reinforcements, which prevents warping information to be transferred from cell to cell. It is stressed that this is a special case given the wall thickness. As described above, the choice of wall thickness was made for the local buckling to occur prior to the column buckling.

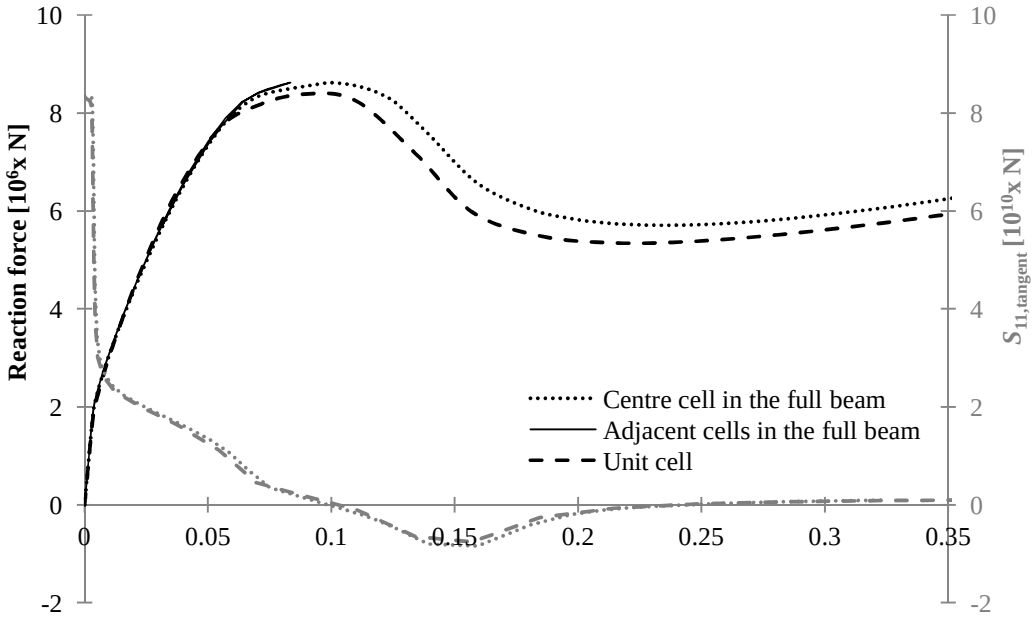

Figure 12: Load (left axis) and tangent stiffness (right axis) as a function of strain

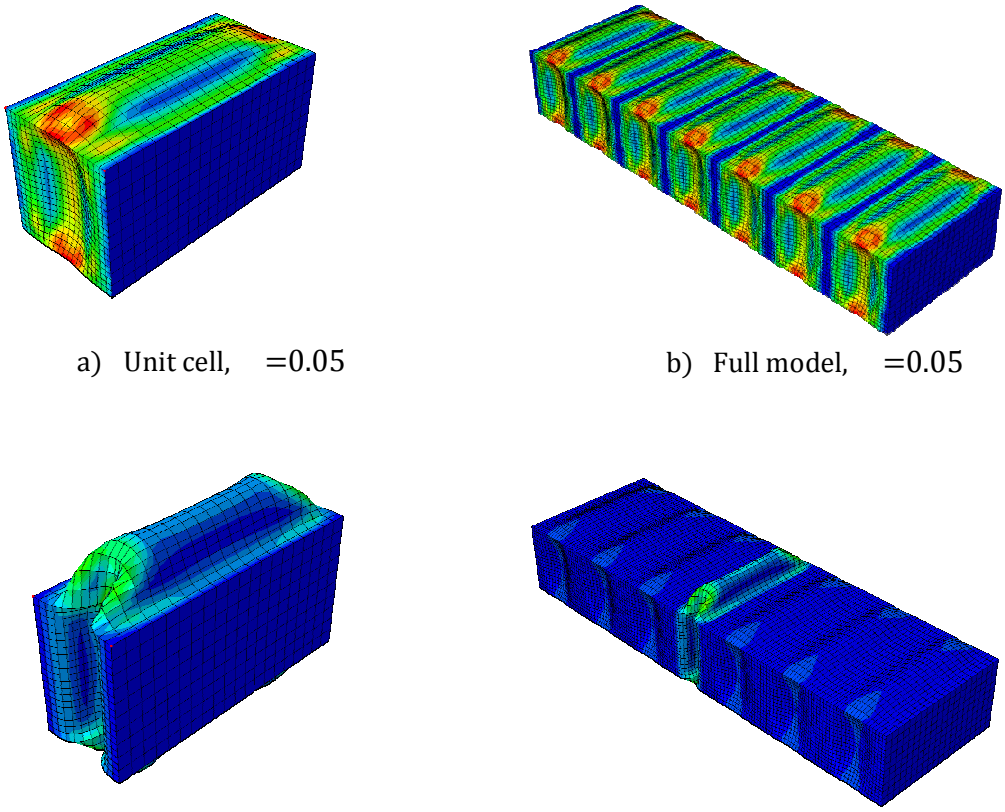

Figure 13: Deformed shapes, with scale factor of one, for the unit cell and the full model of the reinforced box beam at different stages of the localisation process (contour plot shows corresponding von Mises stress)

4.4. Active Twist Rotor blade modelled with tie constraints

The ATR blade from NASA and MIT brings a higher level of complexity (both in the material and geometrical definitions) which allows further verification of the approach. The dimensions of the cross section are depicted in Figure 14 and its material properties described in Table 4. More details can be found in Cesnik and Ortega (1999). The cross section has been modelled without the foam core, and extruded to a total depth of 20% the maximum cross-sectional dimension. Note, however, that the results are independent of that second selection. It is worth noting the current method allows for various features of the FEM package to be used in the solution. In this case, the various parts of the section (skin, spars, joints, etc.) were meshed independently ,without the need for coincident meshes on the interface, and were assembled using Abaqus tie constraints (SIMULIA, 2010) for a mesh transitioning between pairs of surfaces. As it was already mentioned, this enhances the scalability and possibilities

of the current solution method, as the details in the connection between spar and skin have a small effect in the homogenized stiffness. The mesh used consists of 3912 C3D8 elements and 6171 nodes which is very similar to that used in UM/VABS (Palacios and Cesnik, 2005). Full integration was used here to mitigate a problem of artificial strain energy creation. The stiffness constants obtained through this method have been summarised in Table 5 and compared to those of Cesnik and Ortega (1999) (VABS-A) and those in UM/VABS (Palacios and Cesnik, 2005). The direct terms are in full agreement with UM/VABS model, and the coupling terms are very accurate. When compared to the results from VABS-A we find a down-to-discretisation agreement for most terms except the torsional stiffness. For this coefficient, the observed discrepancy is ~5% but this has been identified in Palacios and Cesnik (2005) as a ply angle orientation error. As it can be seen, the tie constraints introduced to link the various model parts have a negligible effect on the solution.

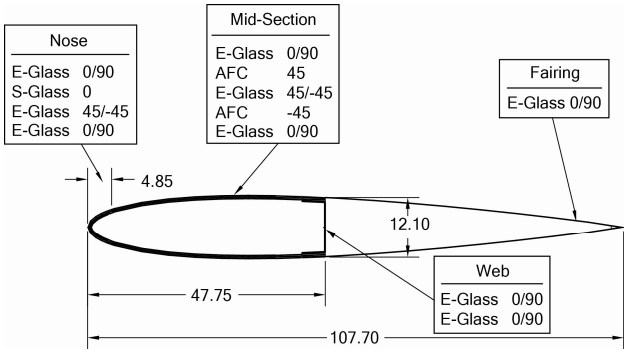

Figure 14: Dimensions (in mm) of the ATR blade with the composite layups

Table 4: Mechanical properties of the ATR wing (Cesnik and Ortega-Morales, 1999)

Material Property	Units	E-Glass (Style 120 Fabric)	S-Glass (Unitape)	Active-Fibre Composite
E_L	GPa	20.7	46.9	22.18
E_T	GPa	20.7	12.1	14.91
G_{LT}	GPa	4.1	3.6	5.13
ν_{LT}	-	0.13	0.28	0.454
t_{PLY}	mm	0.114	0.229	0.203

Table 5: Stiffness constants comparison between different methods

Stiffness constant *(% diff w.r.t. present method)*	**VABS-A**		**UM/VABS**		**Present method**
S_{11} [N]	1.684	*-0.42%*	1.677	*-0.06%*	1.676
S_{22} [Nm²]	34.7	*0.06%*	34.79	*-0.06%*	34.77
S_{33} [Nm²]	41.64	*-1.18%*	41.18	*-0.07%*	41.15
S_{44} [kNm²]	1.031	*5.04%*	1.086	*-0.28%*	1.083
S_{12} [Nm]	-13.07	*-1.68%*	-12.89	*-0.31%*	-12.85
S_{14} [Nm]	250.7	*-0.76%*	249.6	*-0.32%*	248.8

5. Conclusion

An approach to obtaining homogenised properties of slender periodic composite structures has been presented. It is based on the equivalence between the strain states at the large and small scales and the conservation of strain energy between both and it can be implemented via periodic boundary conditions in an off-the-shelf finite element code. The use of a 3-D unit cell does not require the assumption of constant cross sections and leads to a more sophisticated analysis of complex-geometry slender structures at a preliminary stage at a very low computational cost. The modelling of the geometry in our implementation is fully parametric which allows sensitivity analysis to be done. The way the loadings are introduced into the model and the final outputs exported make this approach readily compatible with engineering beam models. The numerical examples show excellent agreement with other available methods and have also demonstrated the suitability of the approach to calculate local buckling strain and the associated reduction of beam tangent stiffness in a beam's unit cell using nonlinear analysis. Overall, this method is a very flexible alternative to obtain the homogenised first-order stiffness constants and local buckling loads of an arbitrarily-shaped periodic composite beam. Application of this approach to high-aspect ratio air vehicle analysis is expected to improve the accuracy of the results in the conceptual stage of design, reducing the time and cost of the whole design process and bringing project inception and flight readiness closer together.

References

Buannic, N., Cartraud, P., 2001a. Higher-order effective modeling of periodic heterogeneous beams. I. Asymptotic expansion method. *International Journal of Solids and Structures* 38, 7139-7161.

Buannic, N., Cartraud, P., 2001b. Higher-order effective modeling of periodic heterogeneous beams. II. Derivation of the proper boundary conditions for the interior asymptotic solution. *International Journal of Solids and Structures* 38, 7163-7180.

Cardona, A., Geradin, M., 1988. A beam finite element non linear theory with finite rotations. *International Journal for Numerical Methods in Engineering* 26, 2403-2438.

Cartraud, P., Messager, T., 2006. Computational homogenization of periodic beam-like structures. *International Journal of Solids and Structures* 43, 686-696.

Cesnik, C., Hodges, D., 1997. VABS: A New Concept for Composite Rotor Blade Cross Sectional Modeling. *Journal of the American Helicopter Society* 42, 27.

Cesnik, C.E.S., Hodges, D.H., Sutyrin, V.G., 1996. Cross-sectional analysis of composite beams including large initial twist and curvature effects. *AIAA journal* 34, 1913-1920.

Cesnik, C.E.S., Ortega-Morales, M., 1999. Active composite beam cross-sectional modeling-stiffness and active force constants. *Proceedings of the 40th AIAA Structures, Structural Dynamics and Materials Conferences. St. Louis, Missouri, AIAA-99-1548*.

Geers, M.G.D., Kouznetsova, V., Brekelmans, W., 2010. Multi-scale computational homogenization: Trends and challenges. *Journal of Computational and Applied Mathematics* 234, 2175-2182.

Ghiringhelli, G.L., Mantegazza, P., 1994. Linear, straight and untwisted anisotropic beam section properties from solid finite elements. *Composites Engineering* 4, 1225-1239.

Hodges, D., 1990. A mixed variational formulation based on exact intrinsic equations for dynamics of moving beams. *International Journal of Solids and Structures* 26, 1253-1273.

Hodges, D., 2003. Geometrically exact, intrinsic theory for dynamics of curved and twisted anisotropic beams. *AIAA Journal* 41, 1131-1137.

Hodges, D., 2005. Nonlinear Composite Beam Theory. AIAA series, Reston, VA.

Ieşan, D., 1986a. On Saint-Venant's problem. *Archive for Rational Mechanics and Analysis* 91, 363-373.

Ieşan, D., 1986b. On the theory of uniformly loaded cylinders. *Journal of Elasticity* 16, 375-382.

Jonnalagadda, Y., Whitcomb, J.D., 2011. Calculation of Effective Section Properties for Wind Turbine Blades, Proceedings of the 52nd AIAA Structures, Structural Dynamics and Materials Conferences. Denver, Colorado, AIAA-2011-1881.

Kaewunruen, S., Chiravatchradej, J., Chucheepsakul, S., 2005. Nonlinear free vibrations of marine risers/pipes transporting fluid. *Ocean Engineering* 32, 417-440.

Kennedy, G.J., Martins, J.R.R.A., 2012. A homogenization-based theory for anisotropic beams with accurate through-section stress and strain prediction. *International Journal of Solids and Structures* 49, 54-72.

Kim, J.S., Wang, K., 2010. Vibration Analysis of Composite Beams With End Effects via the Formal Asymptotic Method. *Journal of Vibration and Acoustics* 132, 041003.

Leamy, M.J., Lee, C.-Y., 2009. Dynamic response of intrinsic continua for use in biological and molecular modeling: Explicit finite element formulation. *International Journal for Numerical Methods in Engineering* 80, 1171-1195.

Lee, C.-Y., Yu, W., 2011. Variational asymptotic modeling of composite beams with spanwise heterogeneity. *Journal of Computers and Structures* 89, 1503-1511.

Li, C., Chou, T.-W., 2003. A structural mechanics approach for the analysis of carbon nanotubes. *International Journal of Solids and Structures* 40, 2487-2499.

Palacios, R., Cesnik, C., 2005. Cross-sectional analysis of nonhomogeneous anisotropic active slender structures. *AIAA Journal* 43, 2624.

Palacios, R., Murua, J., Cook, R., 2010. Structural and Aerodynamic Models in Nonlinear Flight Dynamics of Very Flexible Aircraft. *AIAA Journal* 48, 2648-2659.

Pinho, S.T., Iannucci, L., Robinson, P., 2006. Physically based failure models and criteria for laminated fibre-reinforced composites with emphasis on fibre kinking. Part II: FE implementation. *Composites Part A: Applied Science and Manufacturing* 37, 766-777.

Qiao, P., Shan, L., 2005. Explicit local buckling analysis and design of fiber–reinforced plastic composite structural shapes. *Composite Structures* 70, 468-483.

Simo, J., Vu-Quoc, L., 1986. A three-dimensional finite-strain rod model. Part II: Computational aspects. *Computer Methods in Applied Mechanics and Engineering* 58, 79-116.

SIMULIA, 2010. Abaqus 6.10 Documentation. © Dassault Systèmes.

Su, W., Cesnik, C.E.S., 2011. Dynamic response of highly flexible flying wings. *AIAA journal* 49, 324-339.